International Journal of Heat and Mass Transfer 52 (2009) 787–795

Contents lists available at ScienceDirect

International Journal of Heat and Mass Transfer

journal homepage: www.elsevier.com/locate/ijhmt

# Experimental and numerical studies of AISI1020 steel in grind-hardening

Jianhua Zhang [a], Peiqi Ge [a,*], Tien-Chien Jen [b], Lei Zhang [a]

[a] School of Mechanical Engineering, Shandong University, Jinan 250061, China
[b] Mechanical Engineering Department, University of Wisconsin-Milwaukee, Milwaukee, WI 53211, United States

ARTICLE INFO

*Article history:*
Received 19 November 2007
Received in revised form 14 June 2008
Available online 1 October 2008

*Keywords:*
Grind-hardening
Numerical study
Surface hardening
Grinding temperature field

ABSTRACT

Currently, most of the researches studying grind-hardening have used Design of Experiments approach to obtain empirical correlations without any in-depth theoretical analyzes. In this paper, a comprehensive numerical model is developed to simulate the temporal and spatial temperature distributions of the workpiece under the dry grind-hardening condition using finite element method. The simulated hardness penetration depth is deduced from the local temperature distribution and time history of workpiece and its martensitic phase transformation conditions. The results from simulations are validated with experiments. The effect of two major grinding parameters, workpiece speed and depth of cut, on the hardness penetration depth are discussed.



## 1. Introduction

In any grinding processes, the heat generated in the grinding process causes the workpiece and wheel temperatures to rise. The high temperatures could cause various forms of thermal damages, such as workpiece burns. In the past, almost all of researchers tried to eliminate the grinding heat in grinding zone to avoid the grinding burns. In this paper, however, a new technology named grind-hardening is introduced. Due to the significant heat generated during the grinding process, the surface temperature of the workpiece, which rose by the grinding heat, is higher than the austenitizing temperature. This is then followed by rapid cooling to achieve the purpose of surface hardening. Simply speaking, this technology utilizes the dissipated heat in grinding zone to harden the surface layer of the workpiece. It is worth noting that this technology has the potential to fully integrate the surface hardening processes, such as flame hardening, laser hardening [1] and so on, into the production line, and thus reducing manufacturing processes and increasing productivity [2–5].

The grind-hardening technology has been widely studied by many researchers [2–4]. Most of the researches studying grind-hardening have used design of experiments approach [e.g., 2–4], by varying processes parameters with a great deal of experiments. However, due to the complexity of grinding processes [6,7], this approach often makes experimental studies with significant degree of uncertainty of the results. In the past, the thermal analysis of grinding process has been performed by using of finite element method in grind-hardening [8–14]. In this paper, temporal and spatial temperature distributions of the workpiece under grind-hardening condition are simulated based on finite element method. The simulated hardness penetration depth is deduced from the local temperature distribution and time history of workpiece and its martensitic phase transformation conditions. The actual experiment of grind-hardening on a steel workpiece, AISI1020, is carried out in grinding machine using surface grinder, M 7120 A. The metallurgical microstructure, depth and hardness of transect phase transformation layer are analyzed. The results from numerical simulations are validated with experimental data. Furthermore, the effect of two major grinding parameters, table speed and depth of cut, on the hardness penetration depth are presented and discussed in details.

## 2. Theoretical analysis

In any grinding processes, the grinding heat generated in the grinding zone is removed by the grinding wheel, workpiece, chips and the grinding fluid. Fig. 1 illustrates a typical horizontal grinding process. In this study, a dry grinding process is pursued since the main purpose is to use the grinding heat to harden the surface. The rate of heat transfer into the workpiece and its subsequent temperature distribution will be studied for the grind-hardening process.

### 2.1. The heat flux into the workpiece

When the grinding wheel cuts into the workpiece along the grinding zone, almost all of the mechanical energy converts into thermal energy [15]. The total grinding energy can be calculated as follows:

* Corresponding author. Tel.: + 86 531 88396436; fax: + 86 531 88392989.
*E-mail address:* pqge@sdu.edu.cn (P. Ge).

0017-9310/$ - see front matter © 2008 Published by Elsevier Ltd.
doi:10.1016/j.ijheatmasstransfer.2008.06.037

**Nomenclature**

| | |
|---|---|
| $P_c$ | The grinding energy unit area, W/mm$^2$ |
| $F_t$ | The tangential force of grinding, N |
| $V_s$ | The wheel speed, m/s |
| $V_w$ | The table speed, m/s |
| $b$ | The grinding width, mm |
| $l$ | The geometrical contact length between the workpiece and the wheel, mm |
| $a_p$ | Depth of cut, mm |
| $d_s$ | The diameter of the grinding wheel, mm |
| $Q_w$ | The heat flux into the workpiece, W/ mm$^2$ |
| $(kpc)_w$ | The workpiece thermal contact coefficient, w/m k |
| $k_g$ | The grain thermal contact coefficient, w/m k |
| $k_x,k_y,k_z$ | The thermal conductivity $x$, $y$ and $z$ direction w/m k |
| $n_x,n_y,n_z$ | The normal direction cosine |
| $t$ | The time, s |
| $r_0$ | The wear flat radius |
| $\theta^e$ | The temperature matrix |
| e | The symbol of matrix |
| $T$ | Transposes the mark |
| $N$ | The interpolating function matrix |
| $n^e$ | The number of the nods in each element |
| $\Gamma_1,\Gamma_2,\Gamma_3$ | The boundary conditions |
| ATL | The austenitizing temperature line |
| $\theta_{wb,s}$ | The workpiece surface temperature |
| *Greek Symbols* | |
| $\alpha$ | The convective heat transfer coefficient |
| $\rho$ | The material density, kg/m$^3$ |
| $c$ | The material specific heat, J/(kg k) |
| $\varepsilon$ | The energy partition of the heat transfer into the workpiece, |

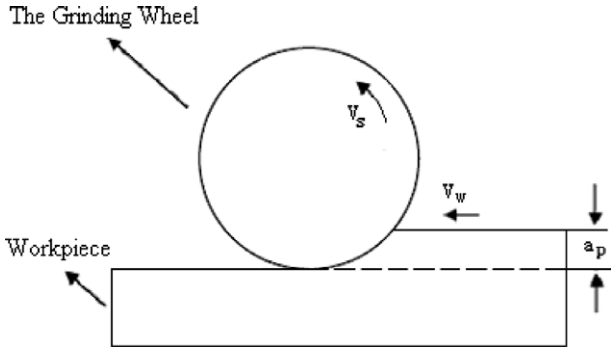


**Fig. 1.** The grinding geometry.

$$P_c = \frac{F_t V_s}{bl} \tag{1}$$

where $P_c$ is the total grinding energy, $F_t$ is the tangential force of grinding, $V_s$ is the wheel speed, $b$ is the grinding width and $l$is the geometrical contact length between the workpiece and the wheel (grinding zone length).

The value of $l$ can be calculated as follow [16]:

$$l = \sqrt{a_p \cdot d_s} \tag{2}$$

where $a_p$ is depth of cut, $d_s$ is the diameter of the grinding wheel.

The heat flux into the workpiece can be described as follow:

$$Q_w = \varepsilon P_c = \varepsilon \frac{F_t V_s}{bl} \tag{3}$$

where $Q_w$ is the heat flux into the workpiece, $\varepsilon$ is the energy partition of the heat transfer into the workpiece. The value of $\varepsilon$ [17] can be estimated as follow:

$$\varepsilon = \left(1 + \frac{k_g}{\sqrt{r_0 V_s}} \times \frac{1}{\sqrt{(kpc)_w}}\right)^{-1} \tag{4}$$

where $(kpc)_w$ is the workpiece thermal contact coefficient, $r_0$ is the wear flat radius;$k_g$ is the grain thermal conductivity.

### 2.2. Mathematical model of the temperature field

Considering the complexity of this technical problem, many of the researchers seek numerical solution by using of the modern mathematics, mechanics theory and the computer. Since the grinding process is mostly in transient state, therefore, the finite element transient temperature field theory of the mathematical model is introduced as follows.

The temperature distribution in the grinding zone is due to the action of many individual grains producing heat at discrete points of the workpiece surface. A method [17,18] that has been widely used in the grinding heat transfer analysis is to consider the temperature distribution to be the superposition of a "background" temperature rise and the "peak" temperature rise which occur only under individual grains. It has been shown experimentally that from the point of view of predicting the metallurgical transformation to the workpiece, it is the workpiece "background" temperature that is of interest, not the peak temperature that occurs under a grain [18]. The reason for this is that the peak temperature occurs for a very short time, and austenitization requires time to occur. The workpiece "background" temperature rise is calculated using the heat entering the workpiece, and distributing in some fashion usually uniform, over the entire grinding zone. In this paper, the workpiece "background" temperature will be simply called workpiece temperature.

The grinding zone is assumed to be a plane heat source with triangular heat flux distribution in the grinding zone. The width of the plane heat source is equal to the width of the workpiece. According to the law of conservation of energy, the general three-dimensional transient heat conduction equation of the grinding temperature distribution in the workpiece can be expressed as,

$$\rho c \frac{\partial \theta}{\partial t} - \frac{\partial}{\partial x}\left(k_x \frac{\partial \theta}{\partial x}\right) - \frac{\partial}{\partial y}\left(k_y \frac{\partial \theta}{\partial y}\right) - \frac{\partial}{\partial z}\left(k_z \frac{\partial \theta}{\partial z}\right) - \rho Q = 0 \tag{5}$$

In order to solve the equation, the following boundary conditions are specified in the computational domain. This computational domain is denoted as $\Omega$. Here, the $\Omega$ region is composed by three kinds of boundary conditions (see Fig. 2 for details):

$\Gamma_1$ boundary condition

$$\theta = \overline{\theta} \tag{6}$$

$\Gamma_2$ boundary condition

$$k_x \frac{\partial \theta}{\partial x} n_x + k_y \frac{\partial \theta}{\partial y} n_y + k_z \frac{\partial \theta}{\partial z} n_z = q \tag{7}$$

$\Gamma_3$ boundary condition

$$k_x \frac{\partial \theta}{\partial x} n_x + k_y \frac{\partial \theta}{\partial y} n_y + k_z \frac{\partial \theta}{\partial z} n_z = \alpha(\theta_a - \theta) \tag{8}$$

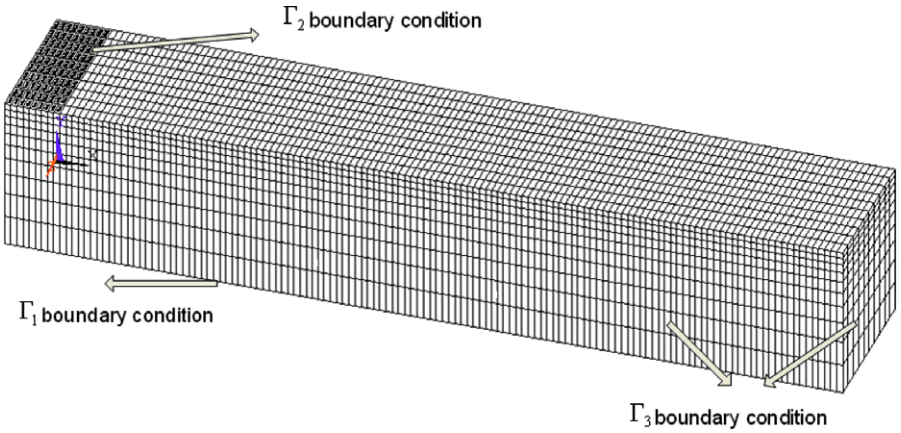


**Fig. 2.** Modeling and meshing.

Here, $\rho$ is the material density; $c$ is the material specific heat; $k_x,k_y,k_z$ is the thermal conductivity in x, y and z direction, respectively.

$Q = Q(x,y,z,t)$ is the internal heat generation; $n_x,n_y,n_z$ is the normal direction cosine; $\overline{\theta} = \overline{\theta}(\Gamma,t)$ is the prescribed temperature on the boundary of $\Gamma_1$; $q = q(\Gamma,t)$ is the heat flux on the boundary of $\Gamma_2$; $\alpha$ is the convective heat transfer coefficient; $\theta_a = \theta_a(\Gamma,t)$ is the ambient temperature; $t$ is the time. For the mathematical and numerical derivation, all the boundary conditions in the $\Omega$ region should meet the following equality.

$$\Gamma_1 + \Gamma_2 + \Gamma_3 = \Gamma \tag{9}$$

The initial condition for the temperature is set to be at ambient temperature for the entire workpiece.

The temperature distribution in the computational domain is not only a function of space but also a function of time. However, the time domain and space domain are not coupled, so some of the discrete and iterative methods can be used in the simulation model. We can establish physical model in discrete spatial domain, while loading in discrete time domain. The mathematical model of temperature field based on the finite element method is established as follow:

$$\begin{aligned}&\sum\nolimits_e \int_{\Omega^e} (\rho c N_i N_j)\theta^e d\Omega \\ &\quad + \sum_e \int_{\Omega^e} \left[\left(\frac{\partial N}{\partial x}\right)^T k_x \frac{\partial N}{\partial T} + \left(\frac{\partial N}{\partial y}\right)^T k_y \frac{\partial N}{\partial y} + \left(\frac{\partial N}{\partial z}\right) k_z \frac{\partial N}{\partial T}\right]\theta^e d\Omega \\ &\quad + \sum_e \int_{\Gamma_3^e} \alpha N_i N_j \theta^e \\ &= \sum_e \int_{\Gamma_2^e} N^T q d\Gamma + \sum_e \int_{\Gamma_3^e} \alpha \theta_a N_i d\Gamma \end{aligned} \tag{10}$$

where, $\theta^e$ is temperature matrix and $T$ denotes the transposes the matrix.$N$represents the interpolating function matrix; $N = [N_1 \quad N_2 \quad \cdots \quad N_{n^e}]$;$n^e$ is the number of the nodes in each element.

## 3. Finite element modeling

### 3.1. Modeling and Meshing

The typical time required for the grind-hardening process is very short (in the order of 0.1 s), thus the grinding heat cannot penetrate deep into the workpiece. The heat affected zone (HAZ) is confined in a small surface layer of workpiece (in the order of mm). However, the entire workpiece is chosen for FEM modeling for completeness. The thermal conductivity and specific heat capacity of the workpiece are considered as variables, which vary with the temperature.

Due to the small heat penetration and high temperature gradient near the surface, the FEM computational domain is discretized using much denser meshes near the surface, and coarse meshes far away from the surface. This can ensure the results from the computation are more accurate. An 8-node rectangle element type is used to model the workpiece. The computational domain is then divided into 10,000 elements with the number of nodes 105,678. The result of the meshing and modeling is shown in Fig. 2.

### 3.2. Loading and solution

After modeling and meshing, the model should be loaded with the specified initial conditions and boundary conditions. Referring to the earlier research [19,20] about grinding heat flux model, the triangular heat flux model is employed in this paper. This is because up grinding cases are considered, in which depth of cut is actually increasing in the grinding direction. The grinding process can then be simulated as the process of the heat flux moves on the surface of the workpiece.

When the model is loaded with a moving heat flux input on the workpiece surface, the time domain is assumed to be discrete. Initially, the grinding heat flux is loaded on the initial region in the grinding zone at first time interval. The heat flux is then loaded on the next region in the grinding area in the next time interval, while the results from the previous time step of the calculation are used as the initial conditions in this step. As this, the heat flux

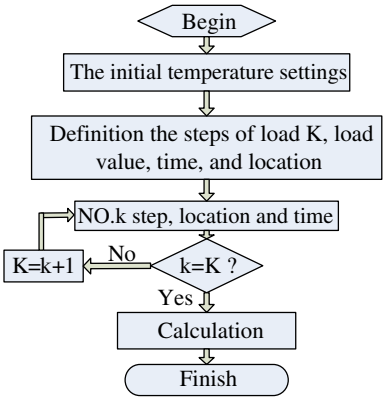


**Fig. 3.** The flow chart of loading.

can move along the surface of the workpiece. The flow chart of loading process is illustrated in Fig. 3. The process of simulation is achieved by using the APDL language. With the inputs of the loading and boundary conditions, the finite element model can be solved.

## 4. Experiment setup

The grind-hardening experiment was performed on a surface grinder, M 7120 A. Fig. 4 shows the actual grind-hardening process in the experiments. The test material used was the AISI1020 steel, which is widely used in many industrial applications. The temperature dependent thermal conductivity and specific heat capacity are as shown in the Fig. 5 (a and b) [9]. The dimensions of workpiece were 10 mm × 10 mm × 80 mm (width × high × length). The chemical composition of the steel is list in Table 1. The grinding conditions are listed in Table 2.

The micro-hardness (HV) of the subsurface is examined on the cross-sectional view samples with a hardness tester. Metallurgical structure is observed on the optical microscope, KH-2200.

## 5. Results and discussion

### 5.1. FEM simulation results

Temperature distribution of the workpiece by the FEM simulation will be discussed in this section. The temperature distribution in grind-hardening was simulated using the corresponding grinding parameters, as shown in Table 2. In this section, only one set of the grind-hardening conditions (underline parameters in the Table 2) was used to illustrate the temporal and spatial temperature distribution in the grind-harding process. In reality, every set of experimental data with corresponding numerical simulation results have been verified with very good agreement. To avoid repeated similar comparisons, only one set of experimental data was used to compare with numerical simulation. The Fig. 6 illustrates the temperature distribution in the workpiece after 1.2 s sparking in. It can be seen from the figure that the temperature decreases quickly in the directions of the thickness, as shown in the Fig. 7. It is observed that the temperature gradient is larger beneath the grinding heat source (into the workpiece), and smaller in behind the grinding heat source. The observed temperature distribution is consistent with other studies on the temperature distribution in the workpiece in up-grinding process [19]. The temperature distribution is also very similar to the other surface hardening technology, such as induction hardening and laser hardening.

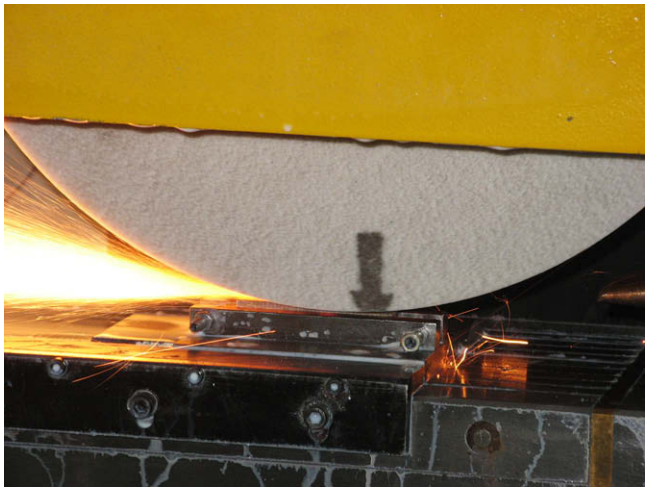

**Fig. 4.** The general view.

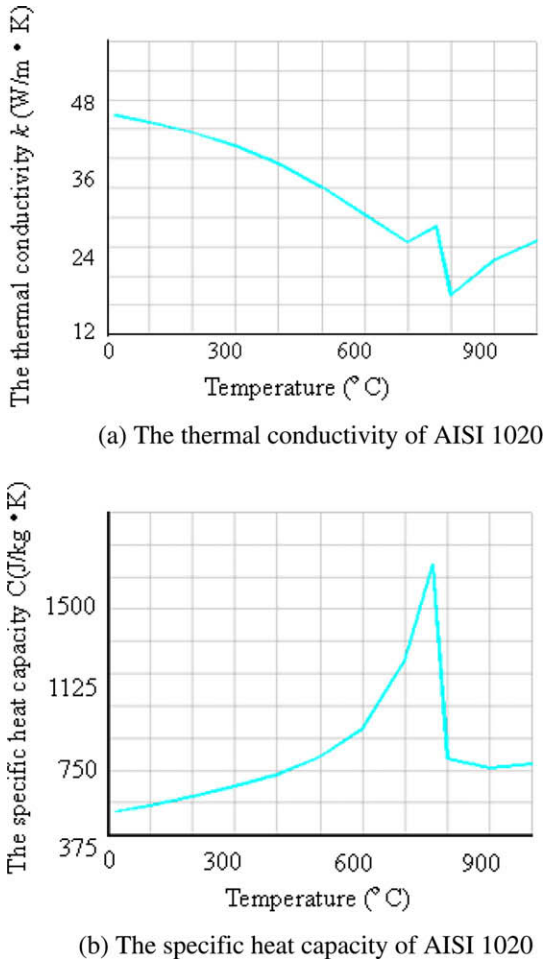


**Fig. 5.** The thermal conductivity and the specific heat capacity of AISI 1020.

**Table 1**
The chemical composition of AISI1020

| Chemical composition AISI1020 [%] | | | | |
|---|---|---|---|---|
| C | Mn | P, max | S, max | Cr, max |
| 0.17 ~ 0.24 | 0.35 ~ 0.65 | 0.035 | 0.035 | 0.25 |

**Table 2**
Grinding conditions

| Wheel | Corundum wheel |
|---|---|
| Wheel diameter | 250[mm] |
| Wheel speed | 19.6[m/s] |
| Table speed | 0.01, 0.03, 0.05[m/s] |
| Depth of cut | 0.1, 0.15, 0.2, 0.3[mm] |
| Environment | Dry grinding |
| Grinding operation | Up-grinding |

The temperature histories at different points into the workpiece (in negative *y*-direction) are shown as Fig. 7. This point location in grinding zone is located at 35 mm in the *x*-direction after sparking in. It can be observed that the highest temperature of the surface is 961 °C. This is when the point of concern just underneath the grinding heat source (or more precisely speaking just at the end of the grinding zone). After reaching the peak temperature at 961 °C, the temperature rapidly decreases to less than 330 °C in

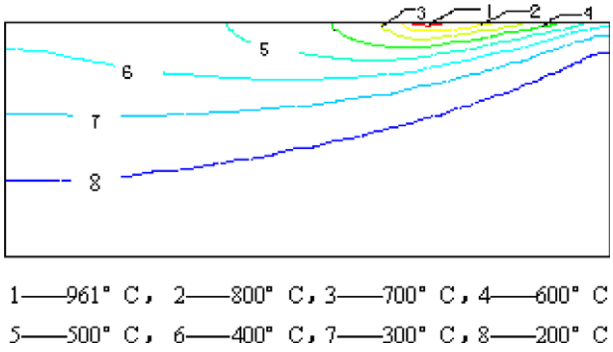


**Fig. 6.** The temperature field.

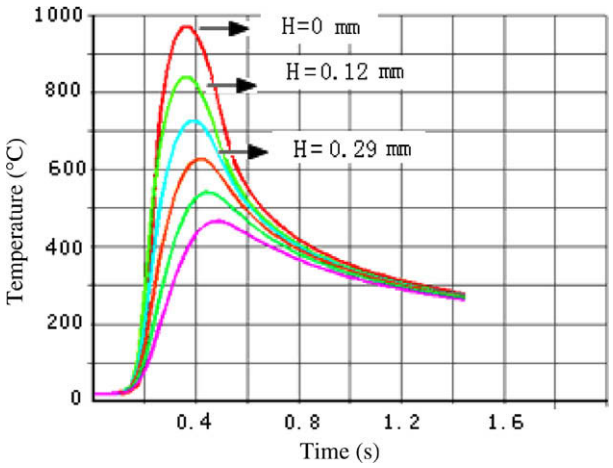


**Fig. 7.** The temperature history.

0.9 second. The simulated temperature history and experimental temperature history are in very good agreement at $H = 0.20$ mm, as shown in the Fig. 8. From the metallographic study of the AISI1020 steel [21], this type of steel can be hardened by heating over 700 °C and cooling below 330 °C in 1.8 s or less. The hardness penetration depth is then predicted by the temperature of history and the metallography of steel. Note that the highest temperature at different depth of the workpiece is different, but all of them are cooled to approximately the same temperature in the same time period (i.e., 1.2 s), as shown in Fig. 7. When the peak temperature at certain depth reaches the austenitic phase transition temperature, the phase transition occurs. In this way, the hardness penetration depth can be predicted. The hardness penetration depth in this calculation was found to be 0.29 mm.

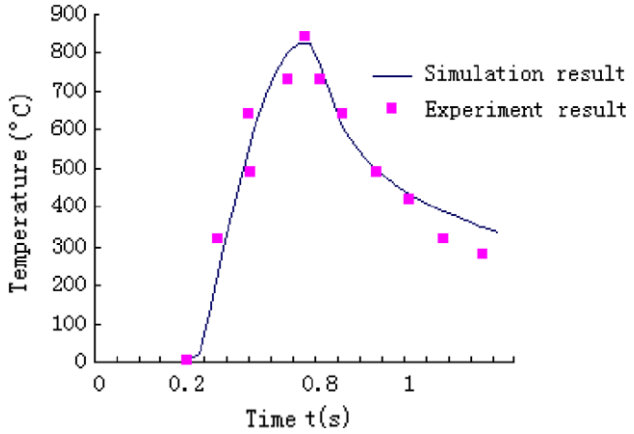


**Fig. 8.** Comparing the simulation result with experiment result at H = 0.20 mm.

### 5.2. Experimental results

After the grind-hardening process, it is found that the average hardness of the bulk material of the workpiece is HV 205, while the surface is HV 660, but the hardness value of the surface workpiece varies. This is because of the uneven distribution of the ferrite and cementite in the workpiece. The micro-hardness (HV) of the subsurface is examined on cross-sectional samples with a hardness tester; the result is shown in Fig. 9. The maximum hardness occurs on the surface of workpiece. The hardness of surface layer goes down slowly along the depth direction. The hardness value of surface layer is observed varying from 520HV to 660HV. The obvious hardness slow-down located at 0.27 mm in the depth direction, and the hardness value changes from 520HV (surface) to 205HV (at ≈0.27 mm). So the hardness penetration depth is determined to be 0.27 from the experiment. The optical micrograph of surface layer after grind-hardening is presented in the Fig. 9. It can be observed from the figure that the matrix microstructure (in the I region of Fig. 10) is the mixture of pearlite and ferrite, which is the original bulk material of the AISI1020. The martensite structure can also be seen on the surface layer of the workpiece (in the IIregion of Fig. 10).

The experimental results have successfully shown that the dissipated heat in the grinding process can be used to harden the workpiece. This technology could have the potential to integrate the surface hardening with surface finishing. From this feasibility study, it seems that the grind-hardening technology could replace conventional surface hardening techniques.

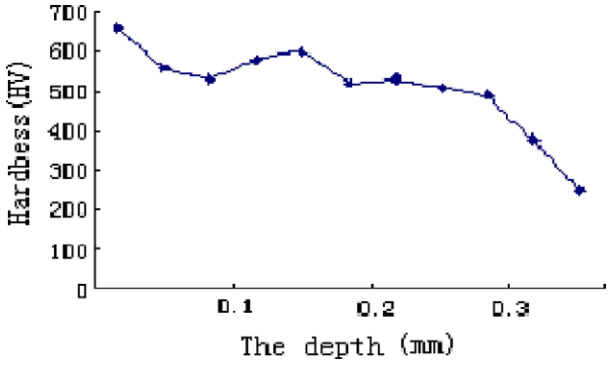


**Fig. 9.** The hardness.

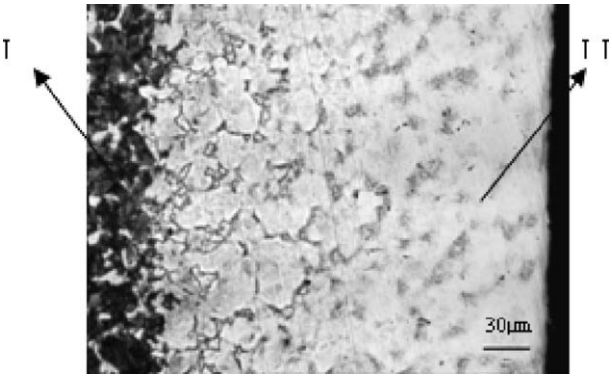


**Fig. 10.** The metallography image.

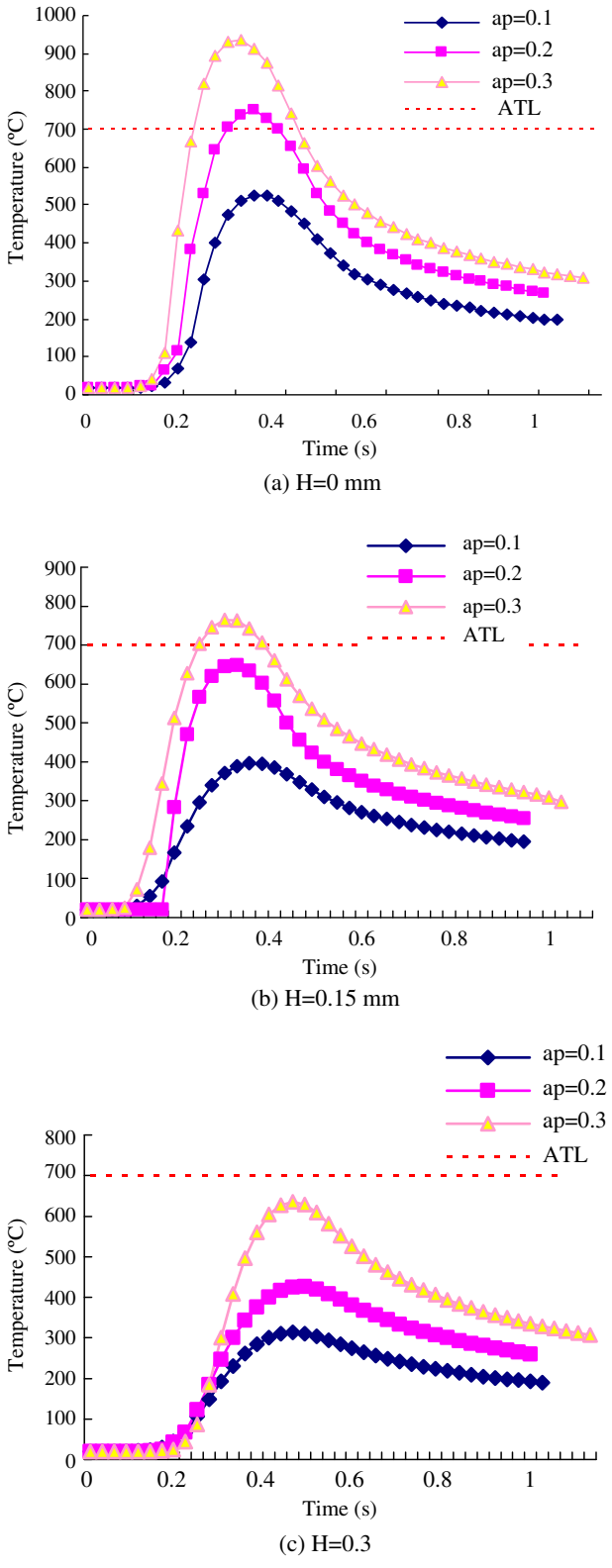


**Fig. 11.** The temperature history in different depth layer.

### 5.3. Compare the simulation with the experiment

According to the martensitic transformation condition of AISI1020, the calculated temperature distribution and its time history of the workpiece can be used to predict the hardness penetration depth. The predicted hardness penetration depth was found to be 0.29 mm, while the hardness measured from the experiment was 0.27 mm. The error is around 7% between the experiment and numerical simulation results. Considering the complexities of this problem, the comparison between experimental data and numerical simulation is in very good agreement.

There are several possible reasons to cause this discrepancy. For example, the measurement errors of the grinding force, the semi-empirical based energy partition and the approximated boundary conditions and initial conditions used in the computational domain are all possible reasons to cause this discrepancy.

### 5.4. The relations between the parameters of grinding and the hardness penetration depth

From discussion above, it has been shown that the hardness of penetration depth of the workpiece can be implicitly predicted by using the finite element simulation of the temperature distribution in the workpiece. The hardness penetration depth of the workpiece is then determined by how deep the grinding temperature penetration depth in the workpiece, in which this temperature is greater than the austenitizing temperature. The temperature distribution is governed by two major parameters of the grinding process; they are workpiece speed and depth of cut. The relation between the parameters of grinding process and hardness of penetration depth will be analyzed and discussed in this section. The grinding wheel speed is set to be at a constant 35 m/s in all the following simulations.

In the first group simulation, the table speed keeps constant at 0.05 m/s. The relation between the depth of cut and the hardness of penetration depth will be uncovered by using of the temperature history of the workpiece. The grind-hardening time of heating and cooling is within 1.2 s. When the temperature rises above the austenitizing temperature line (700 °C; dashed line in Figs. 11 and 13), the surface layer hardening would occur according to the previous analysis. The temperature histories of different depth of cut at different depth of the workpiece are shown in Fig. 11(a–c). Fig. 11(a) illustrates the workpiece surface temperature distribution at three different depths of cut at 0.1 mm, 0.2 mm and 0.3 mm. It is worth noting that the heat penetration depth (and therefore the workpiece temperature) of the workpiece increases with the increasing depth of cut due to larger materials removal rate, which consumes larger grinding energy. Larger grinding energy input also means higher maximum temperature could be achieved by the grinding process. For the curve of the depth of cut of 0.1 mm, the maximum temperatures of the workpiece surface is 520 °C, which is lower than the austenitizing temperature (700 °C), so the surface cannot be hardened. As the depth of cut increases to 0.2 mm, the maximum surface temperature reaches 770 °C, which exceeds the austenitizing temperature. This indicates that the surface could be hardened. Finally, as the depth of cut increases to 0.3 mm, the maximum workpiece temperature becomes 934 °C, which is far above the required austenitizing temperature. Again, this ensures the occurrence of the surface hardening layer. Note that for this case ($a_p$ = 0.3 mm) the time period for the surface temperature larger than the austenitizing temperature is about 0.32 s compares to 0.1 s for the case of $a_p$ = 0.2 mm. Note that austenitizing time plays an essential role in the metallurgical transformation. Compare with other surface hardening technologies, the austenitizing time of grind-hardening in this study is shorter than the austenitizing time of the conventional hardening technology. The austenitizing times of grind-hardening are within 0.5 s in our cases. Fig. 11(b) demonstrates the temperature history at a depth of 0.15 mm into the workpiece. It is interesting to note that for the largest depth of cut, 0.3 mm, the peak temperature at this depth is still above the austenitizing temperature, while the other two depths of cut case, 0.1 mm and

0.2 mm, fall below the required temperature for austenitization. This means that only the case with depth of cut at 0.3 mm could have a hardened layer depth larger than 0.15 mm. As the depth increases to 0.3 mm into the workpiece, all the temperature in the workpiece fall below 700 °C, which is unable to harden the workpiece material at this depth. Thus, it can be concluded that the larger of the depths of cut could result in larger penetration depth of the hardened layer. The predicted hardness of penetration depth versus the depths of cut is summarized in Fig. 12.

In the second group of numerical simulations, the depth of cut keeps constant at 0.3 mm. The effect of the table speeds on the thermal penetration depth is investigated. Fig. 13 (a–c) depict the temperature history of the center points at different depth of the workpiece with three different table speeds, 0.01, 0.03 and 0.05 m/s. Fig. 13(a) illustrates the temperature distributions on the workpiece surface ($H$ = 0.0 mm) at three different table speeds. It can be seen that the surface temperature has a nonlinear behavior. The maximum temperatures are 848, 960C and 934 °C, which correspond to the table speeds of 0.01, 0.03 and 0.05 m/s, respectively. This can be explained as follows. The maximum temperature on the workpiece surface (workpiece background temperature) depends on the grinding power and the table speeds [22,23]. It can be expressed as follows:

$$\theta_{wb,s} = Q_w \sqrt{\frac{4l}{\pi (kpc_p) V_w}} \tag{11}$$

Here, $\theta_{wb,s}$ is the workpiece surface temperature (i.e., workpiece background temperature), $Q_w$ is the heat flux that enters the workpiece and $l$ is the grinding zone length. It can be seen from Eq. (11) that the workpiece temperature is linearly proportional to the heat flux that enters the workpiece and inversely proportional to table speed with negative one half power ($\sim V_w^{-1/2}$). The larger table speed implies larger grinding power input, and thus more thermal energy entering the workpiece, which should increase the workpiece temperature. However, larger table speed also implies shorter time for the heat source to stay on the workpiece surface, thus results in lower temperature. This combination effect shows that there is a maximum temperature under the influence of these two parameters. A simple calculation based on the equation provided above shows that the maximum temperatures are 840, 949 and 932 °C for the same cases illustrated above. This is in very good agreement with the numerical simulation results (848, 960 and 934 °C). It can also be seen from Fig. 13(a) that comparing to depth of cut, the effect of table speeds have a much smaller impact on the maximum temperature. It is worth noting that for all three table

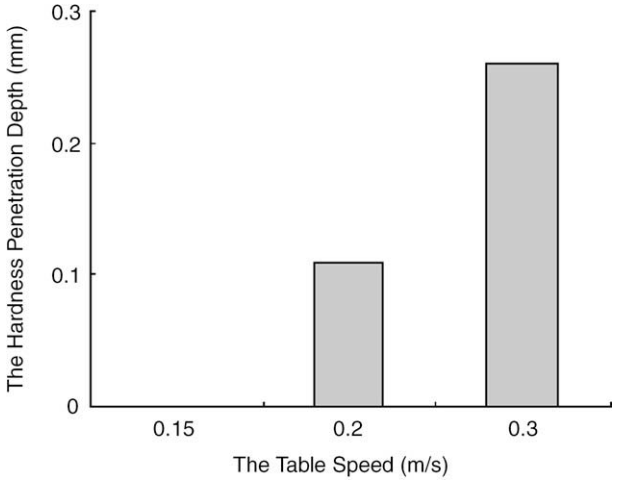


**Fig. 12.** The depth of cut vs. the hardness penetration of depth.

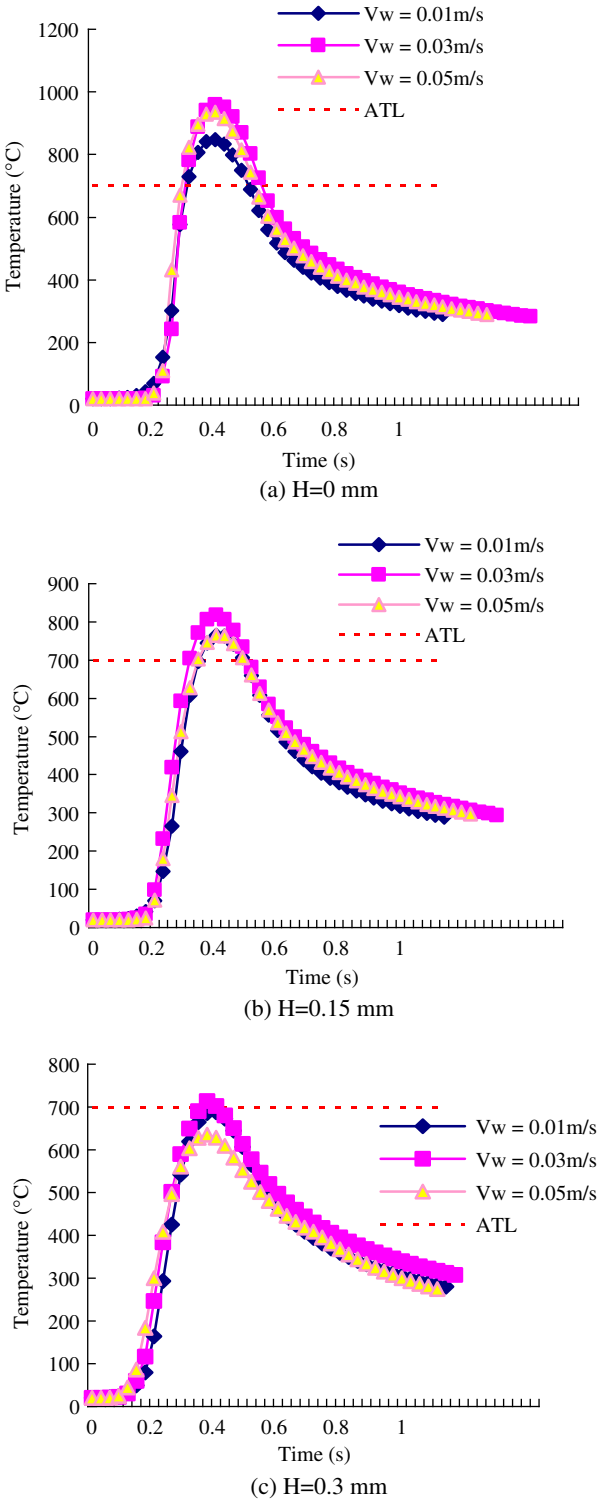


**Fig. 13.** The temperature history in different depth layer.

speeds shown in the figure, the maximum temperatures are all well above the austenitizing temperature, and thus the workpiece surface layer could be hardened. Fig. 13 (b and c) illustrate the temperature history for the case of workpiece depths at 0.15 and 0.30 mm, respectively. It can be seen from the figure that at $H$ = 0.15 mm, the maximum temperatures for all three table speeds are still over the required austenitizing temperature, which means that hardened layer can reach at this depth. However, as the depth increases to 0.3 mm (Fig. 13c), essentially the maximum temperatures for all

three table speeds run below the austenitizing temperature. This indicates that the hardness penetration depth is around 0.3 mm, which is in agreement with the experimental observations. The predicted hardness of penetration depth results with different table speeds is shown in Fig. 14.

Fig. 15 demonstrates the relation between depths of cut and table speed on the possible threshold of successful grind-hardening process on the steel AISI1020. The square symbol denotes the experimental data with successful grind-hardening layer observed in the workpiece, while triangular symbol represents the cases without hardened layer after grinding process. Numerical calculations of workpiece surface temperature are performed on all nine points' data corresponding to the exact experimental conditions. It is then further assumed that the surface layer could be hardened if the workpiece surface temperature exceeds the austenitizing temperature (i.e., 700 °C). The solid line in Fig. 15 denotes the threshold for the onset of the surface hardening after grinding process. This line is obtained by interpolating the temperatures to the austenitizing temperature (i.e., 700 °C). A correlation can be found using curve fitting as follows:

$$f(V_w, a_p) = 25V_w^2 - 3.5V_w - a_p + 0.2925 \quad (12)$$

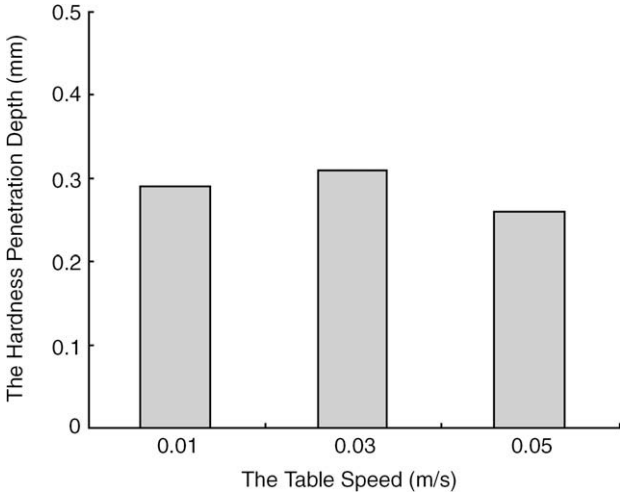


**Fig. 14.** The table speed vs. the hardness penetration of depth.

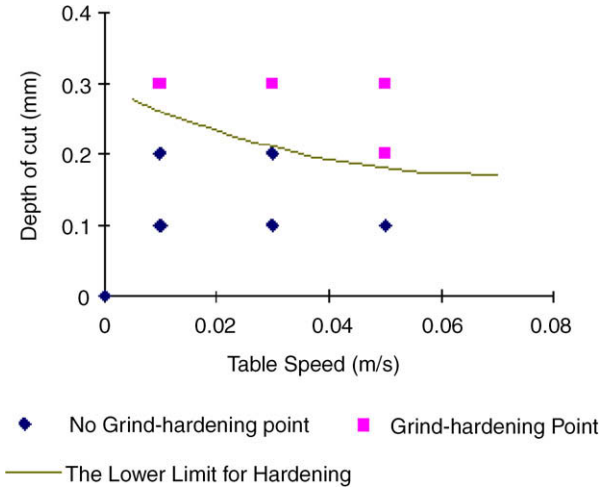


**Fig. 15.** Prediction of the occurrence of grind-hardening.

As can be seen from the equation, the onset of the grind-hardening is determined by the function $f(V_w,a_p)$, which depends on the table speed and depth of cut. If $f(V_w,a_p) = 0$, the parabolic curve in Fig. 15 is the threshold of the onset of the grind-hardening in the workpiece. If $f(V_w,a_p) > 0$, it means the workpiece surface could undergo the surface hardening, while $f(V_w,a_p) < 0$ indicates no hardening layer after the grinding process.

## 6. Conclusion

In this study, the surface of AISI1020 steel has been successfully hardened by the grind-hardening technology. It is found experimentally that the martensitic transformation occurred in the surface layer of workpiece after grind-hardening process. The experimental result shows that the hardness penetration depth is around 0.27 mm. Spatial and temporal temperature distributions are simulated based on finite element method. The simulated hardness penetration depth is derived from the temperature of workpiece and martensitic phase transformation conditions. The numerical simulation results predict a 0.29 mm hardness penetration depth for the same grind-hardening condition as the experiments, which is in very good agreement with the experimental measurement. A parametric study is also performed on the effect of grinding parameters on the hardness depth in the workpiece. The results indicate that the two major grinding parameters, depth of cut and table speed, have significant influence on the hardness of penetration depth. A correlation for the threshold of the onset of hardening after grinding is presented. From this feasibility study, it can be concluded this technology has the potential to integrate the surface hardening processes into the production line, and thus reduce manufacturing processes and increase productivity.

## Acknowledgements

The authors acknowledge the support from National Science Foundation of China under the contract of 50675121 and China Scholarship Council. Dr. Tien-Chien Jen acknowledge the partial support from RGI2 of University of Wisconsin-Milwaukee, US EPA award RD-833357 and NSF CMMI 0739503.

## References

[1] S. Bin-Mansoor, B.S. Yilbas, Laser pulse heating of steel surface: consideration of phase-change process, Numerical Heat Transfer Part A: Applications 50 (2006) 787–807 (21).
[2] E. Brinksmeier, T. Brockhoff, Utilization of grinding heat as a new heat treatment process, Annals of the CIRP 45 (1996) 283–286.
[3] T. Brockhoff, Grind-hardening: a comprehensive view, Annals of the CIRP 48 (1999) 255–260.
[4] P. Ge, J. Sun, Z. Liu, Grinding hardening—integration manufacturing technology of grinding and surface heat treatment process, Tool Engineering 35 (2001) 7–10.
[5] K. Salonitis, G. Tsoukantas, S. Drakopoulos, P. Stavropoulos, G. Chryssolouris, Environmental impact assessment of grind-hardening process, Proceedings of the 13th CIRP International Conference on Life Cycle Engineering (2006) 657–662.
[6] Jianhua Zhang, Peiqi Ge, Lei Zhang, Research on the grinding force based on the probability statistics, China Mechanical Engineering 18 (2007) 2399–2402.
[7] G. Chryssolouris, K. Salonitis, Theoretical investigation of the grinding wheel effect on grind-hardening process, Proceedings of the IFAC Conference on Manufacturing Management and Control (2004) 13–18.
[8] L. Zhang, P.Q. Ge, J.H. Zhang, Z.J. Zhu, Z.Y. Luan, Experimental and simulation studies on temperature field of 40Cr steel surface layer in grind-hardening, International Journal of Abrasive Technology 1 (2) (2007) 187–197.
[9] Lei Zhang, Study on mechanism and experiment of single-pass surface grind-hardening technology, Ph.D Thesis, Shandong University, 2006.
[10] Jianhua Zhang, Peiqi Ge, Lei Zhang, Theory investigation for temperature field in grind-hardening technology, Tool Engineering 41 (2007) 14–16.
[11] G. Chryssolouris, K. Tsirbas, K. Salonitis, An analytical and numerical approach to grind-hardening, SME Journal of Manufacturing Processes 7 (1) (2005) 1–9.
[12] K. Salonitis, G. Chryssolouris, Cooling in grind-hardening operations, International Journal of Advanced Manufacturing Technology 33 (3-4) (2007) 285–297.

[13] K. Salonitis, G. Chryssolouris, Thermal analysis of grind-hardening process, International Journal of Manufacturing Technology and Management 12 (1/2/3) (2007) 72–92.
[14] K. Salonitis, P. Stavropoulos, G. Chryssolouris, Finite element modeling of grind hardening process, Proceedings of the 10th CIRP International Workshop on Modeling of Machining Operations (2007) 117–123.
[15] B. Li, B. Zhao, Modern Grinding Technology, China Machine Press, 2003.
[16] L.C. Zhang, T. Suto, H. Noguchi, T. Waida, Applied mechanics in grinding, International Journal of Machine Tool & Manufacture 33 (1993) 587–597.
[17] R.S. Hahn, The relation between grinding conditions and thermal damage in the workpiece, Transactions of the ASME 78 (1956) 807–812.
[18] W.B. Rowe, M.N. Morgan et al., Validation of thermal properties in grinding, CIRP Annals, vol. 50, pp. 205–208.
[19] T.C. Jen, A.S. Lavine, A variable heat flux model of heat transfer in grinding: model development, ASME Journal of Heat Transfer 117 (1995) 473–478.
[20] M. Mahdi, L.C. Zhang, Applied mechanics in grinding-IV. The mechanism of grinding induced phase transformation, International Journal of Machine Tools and Manufacture 35 (1995) 1397–1409.
[21] Z. Hu, The Curves Handbook of the Steels Heat Treatment, National Defense Industry Press, 1986.
[22] A.S. Lavine, T.C. Jen, Thermal aspects of grinding: heat transfer to workpiece, wheel, and fluid, ASME Journal of Heat Transfer 117 (1991) 296–303.
[23] A.S. Lavine, T.C. Jen, Coupled heat transfer to workpiece, wheel, and fluid in grinding, and the occurrence of workpiece burn, International Journal of Heat and Mass Transfer 34 (4/5) (1991) 983–992.